High-Pressure Potato Starch Granule Gelatinization: Synchrotron Radiation Micro-SAXS/WAXS Using a Diamond Anvil Cell

R. Gebhardt, M. Hanfland, M. Mezouar, and C. Riekel*

European Synchrotron Radiation Facility, B.P. 220, F-38043 Grenoble Cedex, France

Received February 6, 2007; Revised Manuscript Received April 16, 2007

Potato starch granules have been examined by synchrotron radiation small- and wide-angle scattering in a diamond anvil cell (DAC) up to 750 MPa. Use of a 1 μm synchrotron radiation beam allowed the mapping of individual granules at several pressure levels. The data collected at 183 MPa show an increase in the *a* axis and lamellar period from the edge to the center of the granule, probably due to a gradient in water content of the crystalline and amorphous lamellae. The average granules radius increases up to the onset of gelatinization at about 500 MPa, but the *a* axis and the lamellar periodicity remain constant or even show a decrease, suggesting an initial hydration of amorphous growth rings. The onset of gelatinization is accompanied by (i) an increase in the average *a* axis and lamellar periodicity, (ii) the appearance of an equatorial SAXS streak, and (iii) additional short-range order peaks.

Introduction

Starch is a plant polysaccharide composed of concentric shells of alternating hard, semicrystalline, and soft amorphous layers[1,2] with amylopectin double helices dominating the crystalline fraction[3] and amylose chains the amorphous fraction. X-ray scattering techniques provide microscopic information on several length scales. Thus, wide-angle X-ray scattering (WAXS) of the semicrystalline material suggests that the crystalline fraction corresponds to the amylose structure[1] with a highly oriented local fibrillar morphology derived by micro-WAXS.[4,5] Small-angle X-ray scattering (SAXS) provides evidence for a lamellar morphology of alternating crystalline and amorphous lamellae through observation of an ≈9 nm long period (*L*) peak.[6,7] Evidence for a lamellar morphology has also been obtained by electron microscopy.[6] Micro-SAXS data on single potato starch granules have been interpreted by a superhelical lamellar model.[8,9] During gelatinization in the presence of water, starch undergoes an irreversible rheological transformation. Gelatinization can be induced thermally[4,10−12] or by high pressure.[13−15] The thermal disordering process has been associated with a helix−coil transition of the side chains.[16,17] The onset of thermal gelatinization has been studied for single potato starch granules using synchrotron radiation (SR) micro-WAXS techniques.[18] A short-range order component preceding gelatinization suggests a two-step process. Evidence for a rupture of the granular shell structure and formation of surface fragments, which are often called "granular ghosts",[11,12] was obtained. It is assumed that high-pressure gelatinization follows the same disordering mechanism based on FTIR spectroscopy and optical techniques.[13−15] These data suggest a midpoint of the gelatinization transition for potato starch at 650 MPa.[19] The aim of the present study is to use SAXS/WAXS techniques to study the high-pressure gelatinization process in situ and derive a microscopic model. The 1 μm synchrotron radiation beam used allows obtaining in-situ local SAXS/WAXS information on individual granules.

* To whom correspondence should be addressed. E-mail: riekel@esrf.fr.

Experimental Section

Samples. Experiments were performed with sieved, air-dry potato starch granules of 70 μm average size.[18] The samples became hydrated upon loading into the high-pressure cell, which contained water as pressurizing medium.

Diamond Anvil Cell. We used a diamond anvil cell (DAC) with 1 mm thick windows, which is optimized for protein crystallography experiments.[20,21] DAC cells have not been used much in the past for SAXS experiments on functional biological samples[22] but usually provide a more compact format and a higher pressure limit than piston-type high-pressure cells.[23−27] Using water for hydrostatic compression the useful pressure range is from atmospheric pressure to about 1000 MPa. We used a 0.25 mm thick Inconel gasket into which a 380 μm hole was machined by electroerosion, which corresponds to a 28.4 nL free volume. The cell was loaded with water into which seven starch granules and a ruby sphere for pressure calibration were placed. The pressure was generated by He gas and measured before and after each experiment using a Raman spectrometer. Experiments were performed at six pressures (183, 445, 563, 650, 665, and 750 MPa) with a relative precision of ±30 MPa.[20,21] Optical microscopy data on a single granule in a separate experiment show that the granule structure is destroyed at 700 MPa (Figure 1C). The variation of the average radius was determined by fitting a polygon to the granule image using the image analysis software analySIS FIVE (Olympus).

Synchrotron Radiation Experiments. Experiments were performed at the ESRF ID13 beamline.[18,28] The beam from an in-vacuum undulator is monochromated to $\lambda = 0.976$ Å by a liquid N_2 cooled Si-111 double crystal and focused by a Kirkpatrick−Baez (KB) mirror system. A high-resolution CCD camera with an X-ray converter screen and a spot resolution of about 0.1 μm was used for optimizing the focus. An effective beam size of about 1×1 μm^2 fwhm (full-width at half-maximum) was determined by a knife-edge scan of a 20 μm diameter Pt aperture at the focal spot position with a beam divergence of about $1_{hor} \times 0.35_{vert}$ mrad.[2] A flux density of up to 3×10^{10} photons/s/μm^2 was determined by a photodiode. The decay of the X-ray beam intensity with time was monitored with a microionization chamber in front of the sample (Figure 2). The exit of the ionization chamber is fitted with a 20 μm diameter Pt aperture, which removes stray radiation generated by the optical system and allows micro-SAXS experiments.[28] The diamond anvil cell was placed on a large-stroke *x*/*y*/*z* translation

10.1021/bm070156s CCC: $37.00
Published on Web 06/06/2007

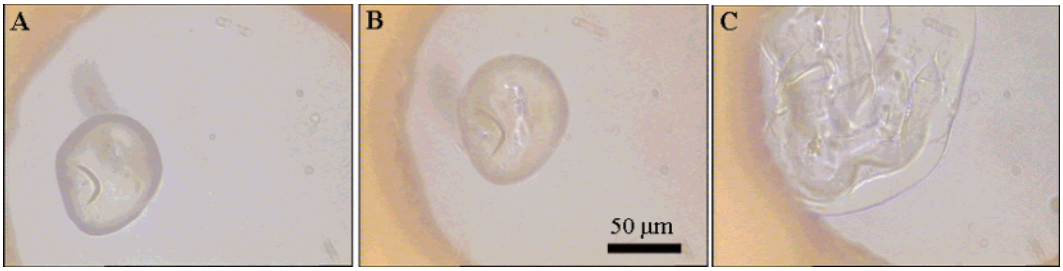

Figure 1. Optical microscopy of starch granule in DAC cell. Intact granules at (A) 300 MPa; at (B) 630 MPa. (C) Gelatinized granule at 700 MPa. The relative precision is ±30 MPa.

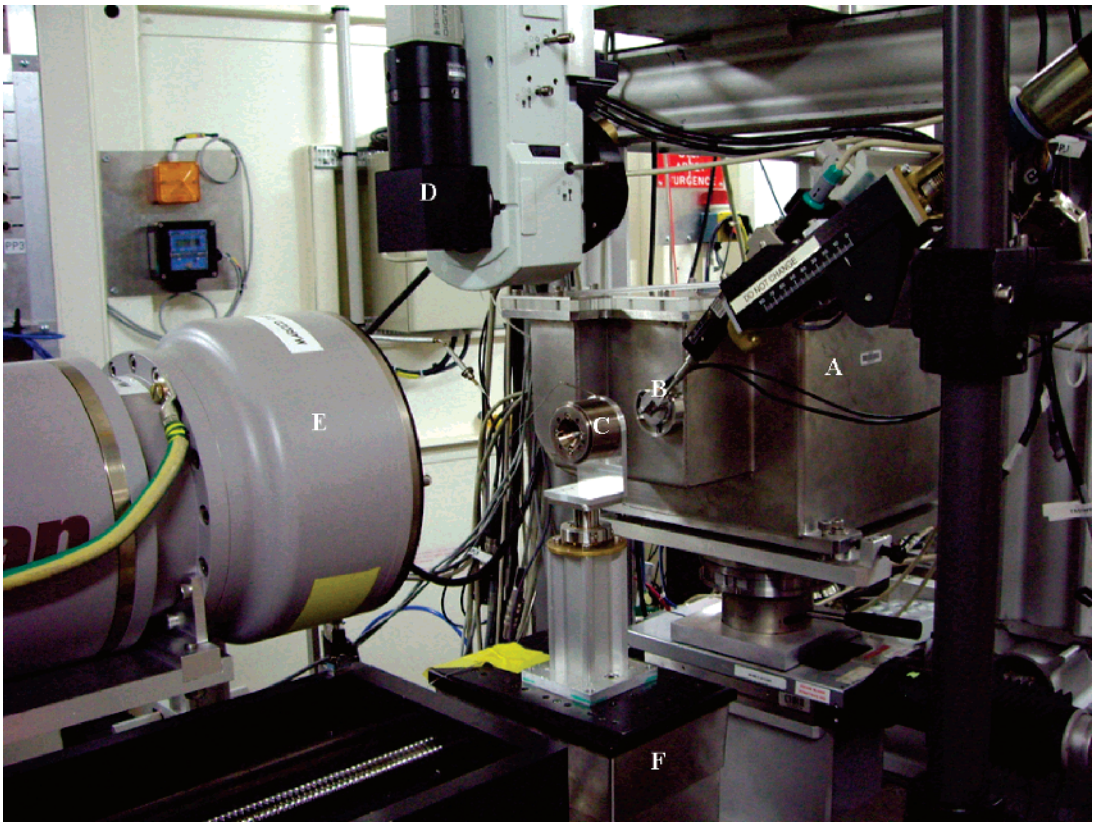

Figure 2. Synchrotron radiation micro SAXS/WAXS setup: (A) mirror chamber; (B) motorized ionization chamber with microaperture; (C) diamond anvil cell; (D) microscope with video camera; (E) MAR165 CCD detection system; (F) vertical translation stage of *x*/*y*/*z* scanning system. A microscope objective is translated into the beam path for optical calibration and sample positioning prior to an experiment.

unit with 400 nm positional repeatability for each axis (Figure 2). The X-ray transmission of the filled cell was about 50%. A motorized lead beamstop of about 200 μm diameter was placed as close as possible to the cell so that SAXS patterns up to about 20 nm could be observed. An Olympus microscope with motorized rotating turret looking upstream along the beam path on the focus position was used for sample alignment in the focal spot with a precision of 1−2 μm normal to the beam axis. This precision is obtained by calibration of the optical system with the microaperture. The granules maintained their position on the diamond window during the experiments. At each pressure level a different granule was chosen and mapped by a mesh scan. The focal spot stability during such a scanning experiment is better than 1 μm, as observed optically by the position of the mesh points for radiation-sensitive samples (e.g., ref 29). The measuring time per pattern was chosen to limit radiation damage as far as possible. Previous experiments on hydrated starch granules have shown that an accumulated dose of 5 photons/nm^3 results in complete destruction of the diffraction pattern.[4] In the current case the accumulated dose was only up to 0.3 photons/nm^3 (calculated for a 70 μm diameter granule and a 1 μm beam). This corresponds to about 1 s exposure time and does not result in a significant reduction of the 100-reflection and hence the crystalline fraction.[18] In practice a constant counting preset value of the ionization chamber was used in order to compensate for the X-ray beam decay. At this dose level one nevertheless optically observes radiation damage, which can destroy the physical integrity of the sample if the mesh points are too close.[4,29] We found that 10 × 10 μm^2 mesh scans resulted in less rupture of the granules than 4 × 4 μm^2 mesh scans. After each mesh step a diffraction pattern was recorded using a MAR165 CCD detector (78.94 μm × 78.94 μm pixel size at the X-ray converter screen; 2K × 2K pixels; 16 bit readout). The sample-to-detector distance was determined to be 158.19 mm by an Al_2O_3 standard.

Data Reduction. The FIT2D software package was used for data reduction and data analysis.[30] The raw pattern with granule scattering overlapping with the background from the DAC cell and liquid scattering is shown in Figure 3A. For background correction a pattern recorded at the edge of the granule was subtracted in order to avoid differences in transmission across the cell as far as possible. This provided a good background subtraction for patterns from the edge of the fiber but introduced a too high liquid background subtraction for the bulk of the granule due to the volume of water displaced by the granule (Figure 3B). For correction, 2D Gaussian profiles were generated, based on the parameters of a Gaussian profile fit of the azimuthally averaged liquid scattering background (Figure 3C). This background was added with a weighting factor to the background

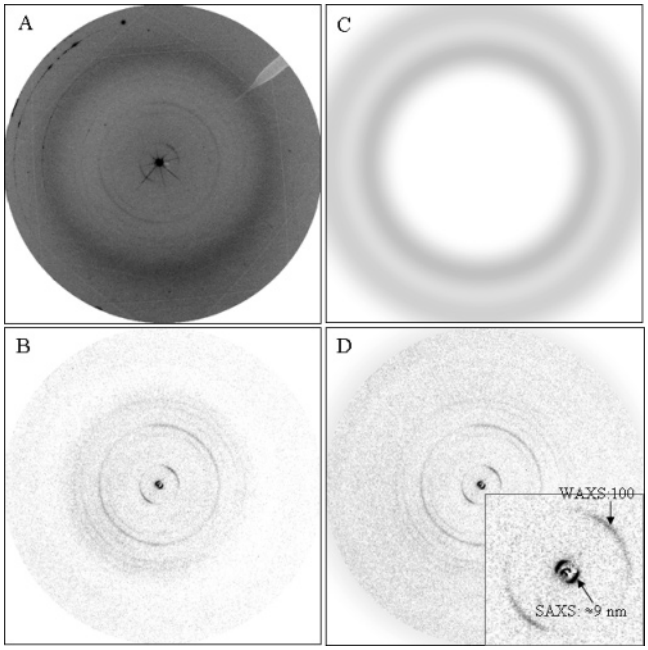

Figure 3. (A) Raw SAXS/WAXS pattern (three patterns averaged) from the edge of a granule at 445 MPa. The variation in pressure is derived from the pressure drift observed across the experimental period. The strongly textured outer arc is due to residual scattering from the Pt microaperture. (B) SAXS/WAXS pattern obtained close to the center of a granule after subtraction of background recorded next to granule. (C) 2D Gaussian profile generated from liquid scattering background. (D) SAXS/WAXS pattern after adding generated 2D Gaussian profile with an empirical weighting factor. The inset shows the range of the 100-reflection (≈1.5 nm) and the SAXS peak (≈9 nm).

corrected pattern (Figure 3D). The weighting factor was empirically chosen to minimize the liquid scattering background peak at $Q = 20.5$ nm^{-1}. The azimuthally averaged profiles of the corrected patterns—shown in Figure 4 for the lowest (183 MPa) and highest (665 MPa) pressure range—are comparable in quality to previous atmospheric pressure, low-temperature data[18] and extend up to $Q \approx 30$ nm^{-1}. The 183 MPa pattern was obtained from four summed patterns recorded within 8 μm from the granule edge, while the 665 MPa corresponds to four summed patterns recorded within 20 μm from the granule edge. The patterns have been simulated by broad Gaussian functions for the short-range order components and narrow Gaussian functions for the B-amylose-type[31] crystalline fraction. We note that the starch-B pattern is still visible at 665 MPa but that additional short-range order peaks suggest partial gelatinization due to melting of crystalline domains. A short-range order peak shifted to larger Q values has also been observed for thermal gelatinization.[18] Crystalline peaks were no longer observed at 750 MPa, where gelatinization had completely destroyed the granule morphology. The diffuse scattering was integrated after instrumental background subtraction in a 30° annular sector with $Q_{min} = 2.4$ nm^{-1}; $Q_{max} = 3.0$ nm^{-1} between the SAXS peak and the 100-reflection. As the annular sector is void of Bragg scattering and the SAXS peak has no diffuse tails, we assume that the integrated background is dominated by incoherent scattering and therefore proportional to the sample volume.

The diffraction patterns obtained from a mesh scan at each specific pressure level can be used to generate a composite image ("diffraction image") where the pixels correspond to a more or less large area of the diffraction pattern. Thus, Figure 5A shows an optical image of the starch granules in the DAC cell at 183 MPa. The diffraction image covering the range of the SAXS peak and the 100-reflection is shown in Figure 5B and the diffraction image for the range of the SAXS peak in Figure 5C. These data show at the same time the hierarchical scales of unit cell (WAXS) and supermolecular organization (SAXS) for single starch granules. Similar ambient pressure data have been reported

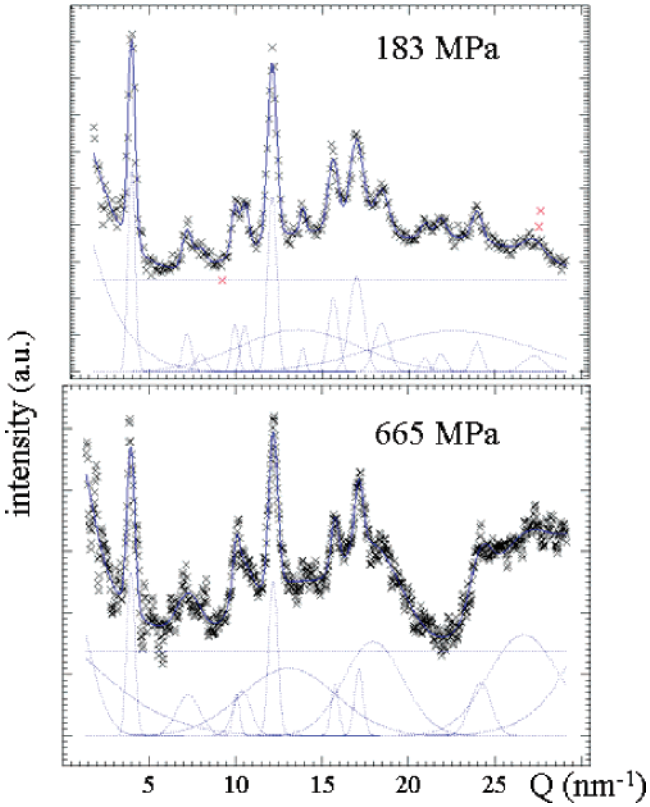

Figure 4. Powder patterns at 183 and 665 MPa fitted by broad Gaussian profiles for the short-range order peaks and narrow Gaussian profiles for the Bragg reflections ($Q = 4\pi \sin \Theta \lambda^{-1}$)

elsewhere.[32] The corresponding images for 650 MPa are shown in Figure 5D−F. The radial organization of granules remains intact up to the highest pressure (Figure 5C,F). No evidence for formation of shell fragments (granular gosts), as observed for thermal gelatinization,[12,18] was obtained. Granules scanned once by a microbeam got squashed at lower pressures than granules, which had not been irradiated (Figure 1). Thus, a granule which had been scanned at 170 MPa got squashed at about 400 MPa. This can be attributed to radiation damage of the granule shell by the microbeam,[4,29] which results in a loss in structural integrity.

Results and Discussion

Homogeneity of Starch Granules. For a quantitative analysis of the granule homogeneity elliptical shells are defined and the normalized frequency of intensities is determined for each shell. This is shown in Figure 6(left) for the diffuse scattering of a granule at 183 MPa. The gradual increase of the normalized frequencies from the edge to the granule center is proportional to the granule volume (Figure 6A; right). Figure 6B shows the same type of plot for the Q_{max} value of the 100-reflection, which is extracted from each pattern by a Gaussian fit. The diffraction image shows that Q_{max} is larger at the edge of the sample than in the center. Such a variation has already been deduced from ambient pressure data.[18,32] The histogram of Q_{max} values from every shell shows an increase in d_{100} spacing by 0.01 nm toward the center of the granule, which corresponds to $\Delta d_{100}/d_{100} \approx 0.006$ (Figure 6B; right). Two in-situ studies on the dependence of the d_{100} spacing as a function of hydration[33,34] support a water gradient toward the center of the granule. It is interesting to note that according to one of the studies[33] a change in d spacing from 1.57 nm (edge) to 1.58 (center) would correspond to a variation of the hydration level from about 20% (edge) to 50% (center). It is therefore tempting to speculate that the inhomo-

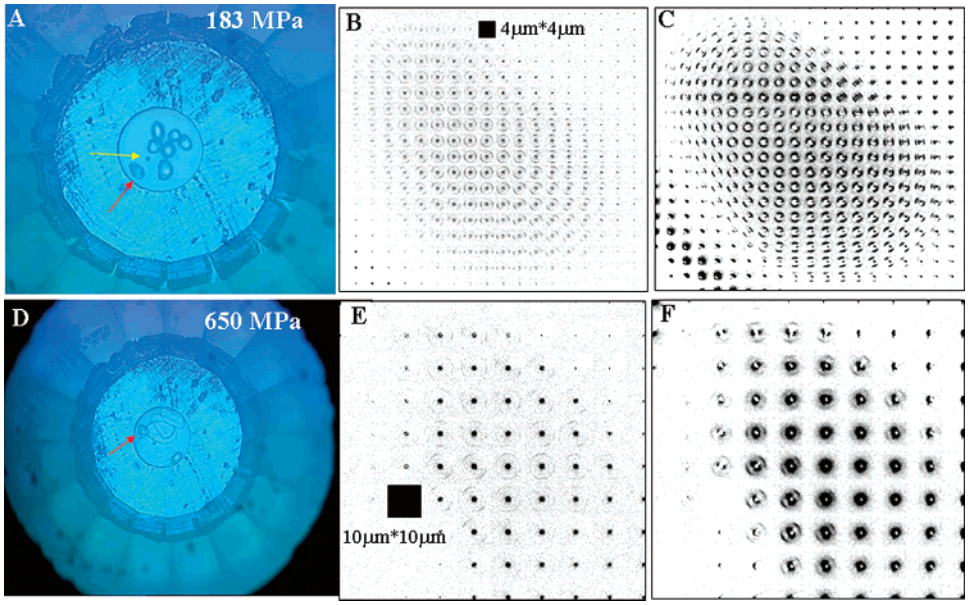

Figure 5. (A) Optical image at 183 MPa; yellow arrow points at the ruby sphere; red arrow points at one of the seven granules which was examined by a 4 × 4 μm^2 mesh scan. (B) Diffraction image composed of pixels covering the range of 100-reflection and SAXS peak. (C) Same for SAXS-peak range. (D) Optical image at 650 MPa; red arrow points to granule examined by a 10 × 10 μm^2 mesh scan. Five of the original seven granules have been squashed. (E) Diffraction image composed of pixels covering range of 100-reflection and SAXS peak. (F) Same for SAXS-peak range.

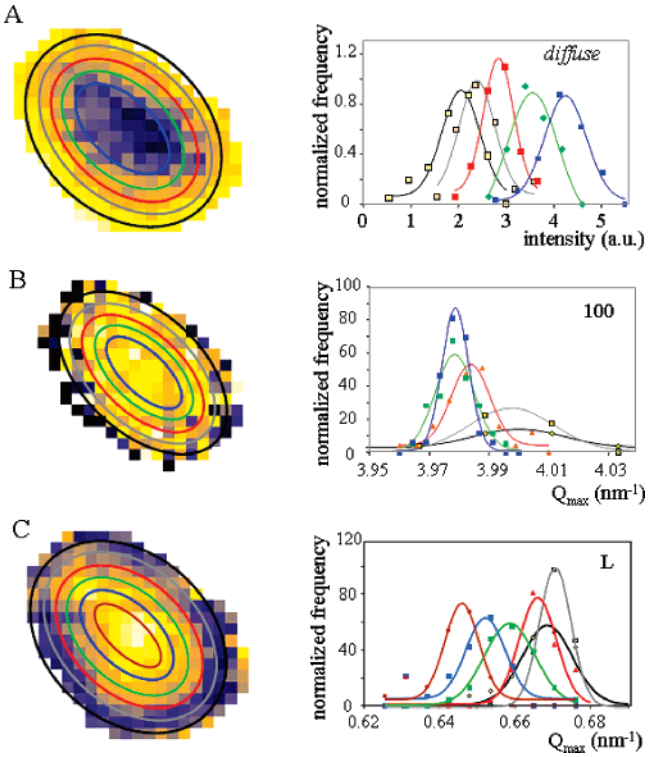

Figure 6. (A) Pseudocolor plot of integrated diffuse scattering intensity (see text) across a granule at 183 MPa. The size of the individual pixels corresponds to 4 × 4 μm^2. Histogram of frequencies of intensity values in the elliptical zones is shown to the right. (B) Pseudocolor plot of Q_{max}-values derived from Gaussian fits to 100-reflections at 183 MPa. Histogram of frequencies of Q_{max}-values in the elliptical zones is shown to the right. (C) Pseudocolor plot of Q_{max}-values derived from Gaussian fit for long period peak at 183 MPa. Histogram of frequencies of Q_{max}-values in the elliptical zones is shown to the right

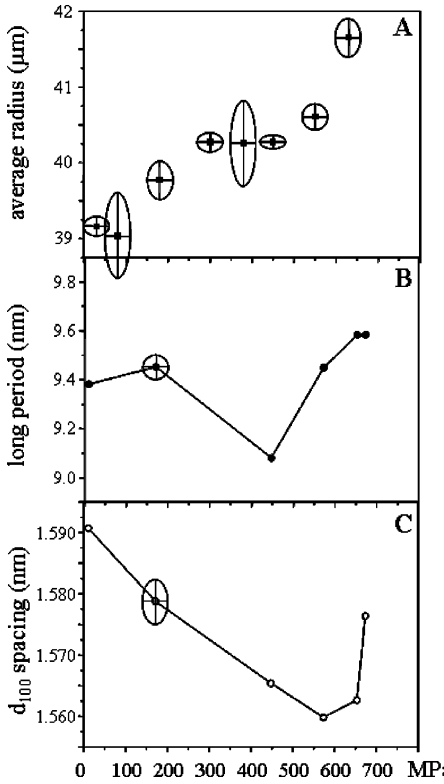

Figure 7. (A) Variation of average granule radius with pressure (squares). (B) Variation of average long period (filled circles). (C) Variation of d_{100} value (open circles) with pressure. The lines are guide lines for the eye. Ambient pressure long period and d_{100} values according to ref 32. The vertical error bars of the average radius are σ values derived from three successive measurements. The vertical error bars (σ) of the long period and d_{100} were derived from a Gaussian fit to the normalized frequencies of the red ellipse in Figure 6B,C. The horizontal error bars correspond to a relative precision of ±30 MPa.

geneous gradient reflects an inhomogeneous amylose distribution,[35,36] although a quantitative re-examination of the d_{100} spacing variation with hydration level for single granules will be required.

In addition to the d_{100} spacing increase we also observe a variation of the SAXS peak across the granule (Figure 6C). The histogram analysis of the long period (L) shows, however, a

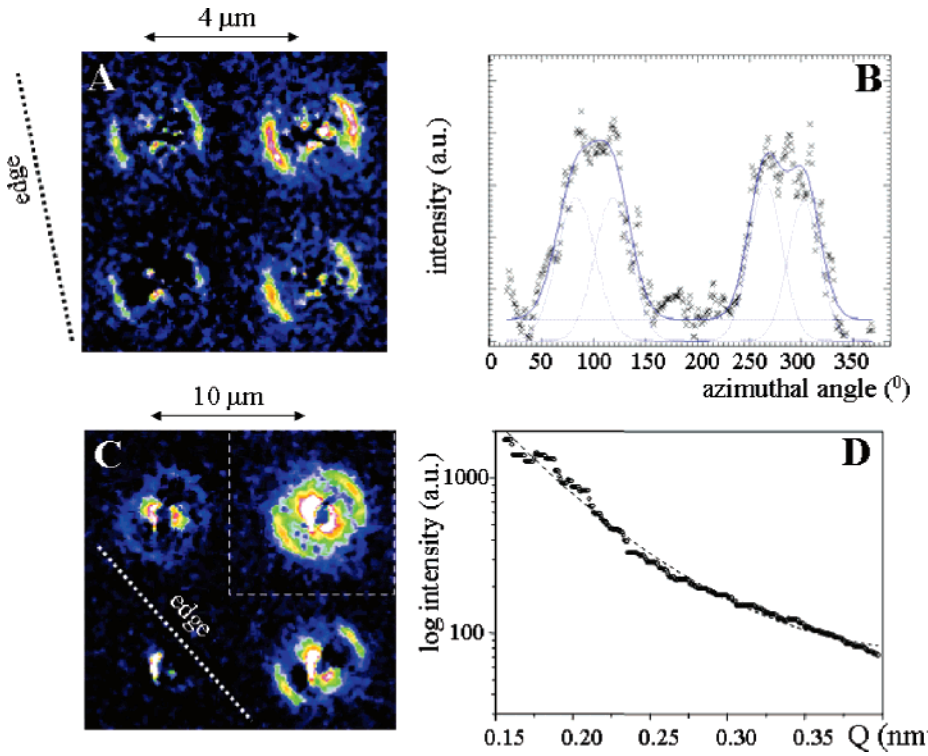

Figure 8. (A) SAXS patterns with meridional SAXS peak from within 8 μm of the edge of a granule at 183 MPa. (B) Azimuthal intensity distribution of the SAXS peak fitted by Gaussian profiles. (C) SAXS patterns from within 20 μm of the edge of a granule at 650 MPa. The edge is schematically shown. (D) Azimuthally integrated equatorial SAXS pattern (hatched rectangle in Figure 8C) at 650 MPa: (circles) experimental data; (hatched line) fit of second-order polynomial.

continuous gradient resembling the volume gradient shown in Figure 6A. The increase of L by 0.36 nm toward the center of the granule corresponds to $\Delta L/L \approx 0.04$, which is significantly higher than the gradient in d_{100} spacing. As the L value can be approximated as the average separation of crystalline domains along the fiber axis, one has to assume that the L gradient across the fiber is dominated by the thickness variation of amorphous domains.

Pressure Effects at Macroscopic and Microscopic Length Scales. The average granule radius shows an increase due to swelling prior to the onset of gelatinization in agreement with other observations[13,14,37] (Figure 7A). This should be compared with the variation in average long period and 100 lattice spacing (d_{100}) (Figure 7B,C). Average ambient pressure values have been added.[32] Both microscopic parameters do not increase prior to the onset of gelatinization, in contrast to the average radius. This suggests that the volume change in this pressure range is principally due to water entering the amorphous growth rings. The decrease of the d_{100} value is nearly linear up to the onset of the gelatinization range, suggesting a simple lattice compression. In contrast, the long period initially decreases and then increases in the gelatinization range. This suggests that in a first step only the amorphous growth rings take up water while the amorphous spacers in the semicrystalline lamellae get compressed. A similar compression has been suggested to occur due to water freezing by SAXS/WAXS.[38] For the onset of thermal gelatinization a compression has been deduced from small-angle neutron scattering (SANS) contrast variation.[10] According to these data the amorphous spacers initially loose water. In the gelatinization range water is also entering the lamellar blocks, which results in an increase of the long period and eventually formation of a disordered phase through disruption of the helical packing. The fact that the radial organization is observed as long as crystalline material is present suggests that gelatinization occurs within granules with intact outer shells.

Onset of Gelatinization. The 2D SAXS patterns obtained prior to the onset of gelatinization show a well-defined SAXS peak and a low background around the beamstop (Figure 8A). The azimuthal intensity distribution of individual SAXS peaks from the edge of the granule can be fitted by double Gaussians (Figure 8B), which supports the model of tilted lamellae.[3,8] The tilt value of 17.9 $\pm$ 0.5° agrees well to the value of 17.25 $\pm$ 0.5° obtained by averaging SAXS patterns from the edges of six granules.[8] The 2D SAXS patterns obtained within the gelatinization range at 650 MPa show an increasing diffuse scattering toward the center of the granule. The diffuse scattering corresponds to a strong equatorial SAXS tail overlapping a random diffuse scattering (Figure 8C). As shown in Figure 8D, the azimuthally averaged SAXS tail can be fitted by a second-order polynomial. Power-law scattering with exponents close to 2 have already been observed for thermal gelatinization and attributed to fractal-like structures.[39] The current data suggest therefore that gelatinization starts with the breakdown of the lateral organization of domains due to an increased mobility of chains while the organization along the local fiber axis appears to be maintained at this step. The onset of pressure-driven gelatinization appears also to be related to the uptake of water by the lamellar structure as evidenced by the increase of both long period and d_{100} spacing (Figure 7B,C). This agrees with the proposed solvation step preceding gelatinization.[15] It is also tempting to speculate that the appearance of a short-range order peak at $Q \approx 18$ nm^{-1} (Figure 4; 665 MPa) reflects the transformation of the helical to a more compact coiled chain conformation.[15]

Conclusion

Potato starch granules show a radial heterogeneity at the micrometer-level as evidenced by gradients in a axis and long period. The micro-SAXS/WAXS data complement optical and

IR spectroscopy results on high-pressure starch gelatinization.[13−15] The increase in granule volume observed prior to gelatinization can be attributed to hydration of the amorphous growth rings as for thermal gelatinization.[40,41] The onset of gelatinization appears to start with hydration of the semicrystalline lamellae and lateral breakdown of crystalline domains. At this stage the external granule shape is still intact. The data support a model suggesting an initial solvation step followed by a helix−coil transition of the molecular chains.[15,42]

The experiments show that it is possible to collect SAXS/WAXS data up to about 1000 MPa in a DAC with a 1 μm synchrotron radiation beam from biopolymer samples. This is an interesting possibility for biopolymer sample quantities, which are only available in small volumes or have to be investigated with high spatial resolution.

Acknowledgment. The authors gratefully acknowledge the help of M. Burghammer in setting up the ID13 beamline. R.G. wishes to acknowledge funding of his position through the FP6 SAXIER grant. C.R. wishes to acknowledge interesting discussions with A. Buléon and H. Lemke.

References and Notes

(1) Buléon, A.; Colonna, P.; Planchot, V.; Ball, S. *Int. J. Mol. Biol.* **1998**, *23*, 85−112.
(2) Gallant, D. J.; Bouchet, B.; Baldwin, P. M. *Carbohydr. Polym.* **1997**, *32*, 177−191.
(3) Oostergetel, G. T.; Bruggen, E. F. J. v. *Carbohydr. Polym.* **1993**, *21*, 7−12.
(4) Buléon, A.; Pontoire, B.; Riekel, C.; Chanzy, H.; Helbert, W.; Vuong, R. *Macromolecules* **1997**, *30*, 3952−3954.
(5) Waigh, T. A.; Hopkinson, I.; Donald, A. M.; Butler, M. F.; Heidelbach, F.; Riekel, C. *Macromolecules* **1997**, *30*, 3813−3820.
(6) Oostergetel, G. T.; Bruggen, E. F. J. v. *Starch/Staerke* **1989**, *41*, 331−335.
(7) Jenkins, P. J.; Cameron, R. E.; Donald, A. M. *Starch/Staerke* **1993**, *45*, 417−420.
(8) Waigh, T. A.; Donald, A. M.; Heidelbach, F.; Riekel, C.; Gidley, M. J. *Biopolymers* **1999**, *49*, 91−105.
(9) Waigh, T. A.; Kato, K. L.; Donald, A. M.; Clarke, C. J.; Riekel, C. *Starch/Stärke* **2000**, *52*, 450−460.
(10) Jenkins, P. J.; Donald, A. M. *Carbohydr. Polym.* **1998**, *308*, 133−147.
(11) Atkin, N. J.; Abeysekera, R. M.; Cheng, S. L.; Robards, A. W. *Carbohydr. Polym.* **1998**, *36*, 173−192.
(12) Atkin, N. J.; Abeysekera, R. M.; Robards, A. W. *Carbohydr. Polym.* **1998**, *36*, 193−204.
(13) Rubens, P.; Goossens, K.; Heremans, K. In *High Pressure Research in the Biosciences and Biotechnology*; Heremans, K., Ed.; Leuven University Press: Leuven, 1997; pp 191−194.
(14) Rubens, P.; Snauwaert, J.; Heremans, K.; Stute, R. *Carbohydr. Polym.* **1999**, *39*, 231−235.
(15) Rubens, P.; Heremans, K. *Biopolymers* **2000**, *54*, 524−530.
(16) Waigh, T. A.; Perry, P.; Riekel, C.; Gidley, M. J.; Donald, A. M. *Macromolecules* **1998**, *31*, 7980−7984.
(17) Waigh, T. A.; Gidley, M. J.; Komanshek, B. U.; Donald, A. M. *Carbohydr. Res.* **2000**, *328*, 165−176.
(18) Lemke, H.; Burghammer, M.; Flot, D.; Roessle, M.; Riekel, C. *Biomacromolecules* **2004**, *5*, 1316−1324.
(19) Stute, R.; Klinger, R. W.; Boguslawski, S.; Eshtiaghi, M. N.; Knorr, D. *Starch/Staerke* **1996**, *48*, 399−408.
(20) Fourme, R.; Girarda, E.; Kahn, R.; Dhaussy, A. C.; Mezouar, M.; Colloc'h, N.; Ascone, I. *Biochem. Biophys. Acta* **2006**, *1764*, 384−390.
(21) Fourme, R.; Kahn, R.; Mezouar, M.; Girard, E.; Hoerentrup, C.; Prangé, T.; Ascone, I. *J. Synchotron Radiat.* **2001**, *8*, 1149−1156.
(22) Czeslik, C.; Malessa, R.; Winter, R.; Rapp, G. *NIM A* **1996**, *368*, 847−851.
(23) Lorenzen, M.; Riekel, C.; Eichler, A.; Häusermann, D. *J. Phys.* **1993**, *3*, 487−490.
(24) Steinhart, M.; Kriechbaum, M.; Pressl, K.; Amenitsch, H.; Laggner, P.; Bernstorff, S. *Rev. Sci. Instrum.* **1999**, *70*, 1540−1545.
(25) Kato, M.; Fujisawa, T. *J. Synchrotron Radiat.* **1998**, *5*, 1282−1286.
(26) Steinhart, M.; Kriechbaum, M.; Pressl, K.; Amenitsch, H.; Laggner, P.; Bernstorff, S. *Rev. Sci. Instrum.* **1997**, *68*, 4588−4592.
(27) Pressl, K.; Kriechbaum, M.; Steinhart, M.; Laggner, P. *Rev. Sci. Instrum.* **1997**, *68*, 4588−4592.
(28) Riekel, C. *Rep. Prog. Phys.* **2000**, *63*, 233−262.
(29) Chanzy, H.; Putaux, J. L.; Dupeyre, D.; Davies, R.; Burghammer, M.; Montanari, S.; Riekel, C. *J. Struct. Biol.* **2006**, *154*, 100−110.
(30) Hammersley, A. In http://www.esrf.fr/computing/scientific/FIT2D/.
(31) Imberty, A.; Pérez, S. *Biopolymers* **1988**, *27*, 1205−1221.
(32) Lemke, H. Correlation between starch synthesis and structure, investigated using synchrotron radiation microdiffraction, Diploma-Thesis, Mathematisch-Naturwissenschaftliche Fakultät; University of Kiel, Germany, 2005.
(33) Cleven, R.; Berg, C. v. d.; Plas, L. v. d. *Starch/Staerke* **1978**, *30*, 223−228.
(34) Buléon, A.; Bizot, H.; Delage, M. M.; Multon, J. L. *Starch/Staerke* **1982**, *34*, 361−366.
(35) Tatge, H.; Marshall, J.; Martin, C.; Edwards, E. A.; Smith, A. M. *Plant Cell Environ.* **1999**, *22*, 543−550.
(36) Kuipers, A. G. J.; Jacobsen, E.; Visser, R. G. F. *Plant Cell Environ.* **1994**, *6*, 43−52.
(37) Douzals, J. P.; Marechal, P. A.; Coquille, K. C.; Gervais, P. *J. Agric. Food Sci.* **1996**, *44*, 1403−1408.
(38) Perry, P. A.; Donald, A. M. *Polymer* **2000**, *41*, 6361−6373.
(39) Vermeylen, R.; Derycke, V.; Delcour, J. A.; Goderis, B.; Reynaers, H.; Koch, M. H. J. *Biomacromolecules* **2006**, *7*, 2624−2630.
(40) Jenkins, P. J.; Donald, A. M. *Polymer* **1996**, *37*, 5559−5568.
(41) Cameron, R. E.; Donald, A. M. *J. Polym. Sci.: B* **1993**, *31*, 1197−1203.
(42) Heremans, K. *Brazilian J. Med. Biol. Res.* **2005**, *38*, 1157−1165.

BM070156S